The effect of air bubbles on optical backscatter sensor measurements under plunging breaking waves.

Iván Cáceres[1], Jose M. Alsina[1], Joep van der Zanden[2, 3], Dominic A. van der A.[4], Jan S. Ribberink[3] and Agustín Sánchez-Arcilla[1]

[1] Laboratori d´Enginyeria Marítima, Universitat Politècnica de Catalunya, Spain.

[2] Offshore Department, Maritime Research Institute Netherlands, Netherlands.

[3] Department of Water Engineering and Management, University of Twente, Netherlands.

[4] School of Engineering, University of Aberdeen, UK.

Keywords: Optical backscatter sensors, air bubbles, breaking waves, laboratory measurements, suspended sediment

Abstract

Accurate suspended sediment concentration measurements are key to understand and quantify the sediment transport patterns in the surf and swash zones. One of the most widely used instruments to collect suspended sediment concentrations is the Optical Backscatter Sensor (OBS). However, the OBS is known to give erroneous readings when deployed in bubbly environments like the surf zone. The present study aims to quantify the influence of an aerated wave breaking environment on the OBS sediment concentration measurements. Experiments are performed in a large wave flume, which ensures full air entrapment under plunging breaking waves, and avoids scale effects that could affect the volume of entrapped air, the air bubble penetration depth and the residence time of air bubbles in the post-breaking turbulent eddies. OBS measurements are obtained at 66 locations along a fixed bed profile for 14 regular breaking wave conditions. In the absence of suspended sediment particles, OBS voltage measurements are used as a proxy for air bubble content. The presented OBS results show peaks up to 1.49 V (31% of the OBS measurement range, corresponding to 16 g/l for sediment with d_{50} = 0.25 mm) produced by air bubbles in the most energetic tested wave breaking conditions, while the maximum time-averaged value obtained is 0.48 V (10% of the OBS measurement range, corresponding to 5 g/l). The results highlight the importance of considering the presence of air bubbles where OBS are deployed to measure suspended sediment concentrations. A good correlation is found between the breaker depth index and the air bubble distribution and two predictive formulas are derived to forecast the area of air bubble influence in the surf zone

1.- Introduction

The nearshore zone is characterized by strong currents and turbulent bubbly flows induced by wave breaking. The dynamics in this region are complex and their understanding is typically hampered by the lack of accurate and reliable measurements. Obtaining detailed measurements of water surface elevation, sediment concentration and sediment and water fluxes within the dynamic, highly turbulent and aerated wave breaking region is both a difficult and costly task [1, 2].

One of the most robust, reliable and frequently used equipment to recover suspended sediment concentrations in the surf and swash zones is the Optical Backscatter Sensor (OBS) [3]. An OBS is an optical sensor that measures turbidity and suspended sediment concentration by detecting the light backscattered from suspended matter. This sensor consist of a high intensity infra-red emitting diode, a detector, and a linear, solid state temperature transducer (D&A Manual, 1991 [4, https://s.campbellsci.com/documents/eu/technical-papers/obs_bubbles.pdf]). The OBS output signal comes as a voltage which is converted to suspended sediment concentration (g/l) by means of a calibration using sediment from the field site [5, 6]. However, light is scattered not only by sediment particles, but also by air bubbles, as the refractive index of air is lower than the refractive index of water. Consequently, high voltage readings by OBSs due to air bubble presence may falsely be interpreted as suspended sediment events. Initial studies describing the performance of OBS sensors [3, 7] reported a negligible influence of air bubbles on the sediment concentration signal. These initial studies, involving bubbles produced by breaking ocean waves, were based on the assumption that the largest air bubbles (those that produce highest backscatter) remain close to the water surface while sediment transport processes occur near the bottom, which means that air bubbles do not significantly affect sediment transport measurements. According to the OBS manual provided by the manufacturer of the OBS-3+ used in the present study (D&A Instrument Company, acquired in 2007 by Campbell Scientific), the effects of bubbles on OBS measurements is minimal [4]. However, several subsequent studies have described non-negligible effects of air bubbles on OBS measurements [8, 9, 10]. Terrill et al. (2001) [8] performed experiments designed to measure the effects of bubble size distribution on the scattered light, and found that there is an increase in light backscatter as the void fraction induced by wave breaking increases. Smith and Mocke (2002) [9] carried out a series of small-scale laboratory measurements showing that air bubbles led to voltage readings that corresponded to sediment concentration measurements up to 0.55 g/l, thus producing an erroneous average increase of 32 % in the sediment concentration signal in their experiments. Puleo et al. (2006) [10] performed an exhaustive experimental study including a variety of air bubble sizes (5 types), different water types (fresh, synthetic and salty) and various kinds of sediment (mud and sand). The measurements, which were conducted in a stirred tank generating air bubbles, showed a 25% increase in the OBS voltage induced by air bubbles in the presence of sand and mud. This increase was even greater in synthetic and salt water due to the longer residence times of air bubbles once the stirring in the tank was stopped.

Air bubble entrainment during wave breaking in the ocean plays a role in several important processes: it controls the transfer of heat and gas (including CO2) at the air-sea interface; it influences the transfer of turbulent energy during breaking; and it affects underwater acoustics. This is why the presence of air bubbles or void fractions in the upper ocean layer has attracted recent research efforts (i.e. Terrill et al. 2001 [8]; Kalvoda et al. 2003 [11]; Mori et al. 2007 [12]; Bell et al. 2017 [13] among many others). In comparison to these open ocean studies, air bubble entrainment studies in the surf zone are rather limited and usually done within laboratory small-scale conditions. Small-scale experiments have some limitations in terms of accurately reproducing the prototype scale air bubble entrainment owing to the difficulty of simultaneously satisfying the similitude requirements of

Reynolds number (the ratio between inertia and viscous forces), Froude number (the ratio between inertia forces and gravity forces) and Weber number (the ratio between inertia and surface tension forces). Most wave experiments are scaled to ensure similitude of Froude number between model and prototype, as surface waves are gravity driven, but this limits the similitude of Reynolds and Weber numbers between prototype and model. If fresh water is used and Froude similitude applied, the viscosity and surface tension that control air bubble dynamics cannot be properly scaled. Chanson et al. (2002) [14] showed that full-scale experiments are required to properly represent the air bubble distribution under breaking conditions when fresh water is used as the experimental fluid. Moreover, the above-mentioned similitude limitations also restrict scaling of the air entrainment volume (void fraction) and momentum of air entrained bubbles within the fluid. The void fraction, size and penetration depth of air bubbles depend on the jet velocity of the plunging breaker. Scaled experiments underestimate the air entrainment velocity, reducing the amount, penetration depth and size of the entrained bubbles. Similarly, the escape velocity of an air bubble from the fluid depends largely on penetration depth and bubble size, which are both significantly affected by the scale of the experiments.

The residence times of air bubbles depend mostly on their size. According to Monahan and Lu (1990) [15] and Deane and Stokes (2002) [16], the life-time of bubbles can be divided into two stages: the first stage where the air bubbles are introduced and fragmented by breaking waves, and the second stage where the bubble plume evolves under the influence of turbulent diffusion, advection, buoyant degassing and dissolution. Lamarre (1993) [17] and Lamarre and Melville (1992) [18] conducted laboratory experiments to demonstrate that bubble plumes experience rapid transformation right after breaking. Their measurements show that the volume of air enclosed in the initial air pocket is preserved for up to 1/4 of the wave period after breaking, and that the plumes lose 95% of the initially entrained air volume during the first wave period after breaking.

The aim of this paper is to investigate the effect of air bubbles on OBS measurements under large-scale (prototype) breaking wave conditions. The focus is on plunging breaking waves, which will produce a larger void fraction and bigger air bubbles than spilling waves [19]. The larger void fractions at breaking will lead to the presence of a greater number of air bubbles at deeper water depths, which are likely to interfere with OBS measurements in the surf zone. Under plunging conditions, which are usually found in laboratory experiments studying barred beach profiles, air bubble entrainment is mainly produced by: i) the interaction of the curling wave jet with the water surface at the plunge point; ii) the air entrapped in the cavity of the collapsing plunging wave; and iii) the splashes and turbulence entrainment produced by the secondary wave [16, 20 and 21]. A new large-scale wave flume dataset is produced involving plunging breaking waves over a barred topography. The experiments involved fresh filtered water and the beach profile consisted of a rigid bottom in the absence of mobile sediments. Therefore, the OBS voltage measurements will depend only on the backscatter caused by the air bubbles. The aim of this data set is to quantify the effect of air bubbles on the OBS voltage signal under a variety of plunging wave breaking conditions, and to provide recommendations for OBS deployment in breaking wave conditions. In order to reach this objective, a predictive formula will be derived to determine the area where air bubbles may affect the OBS readings.

2.- Experimental Procedure

2.1 Experimental set-up and measuring equipment

The experiments were performed in the CIEM wave flume at the Catalonia University of Technology (UPC) in Barcelona, a 100 m long, 3 m wide and 4.5 m deep large-scale wave flume. Figure 1 shows the rigid concrete bed profile, as well as the OBS and the water surface elevation measurement positions. All test conditions had a still water level at the toe of the wave paddle of 2.65 m. The bottom profile started with a flat section of 35 m followed by a 1:12 offshore slope and a breaker bar with a water depth at the bar crest of 0.81 m. The bar trough had a water depth of 1.46 m (solid black line shown in Figure 1) and was followed by a 10 m long gentle slope (1:125) until the profile reached a parabolic dissipative profile with an average slope of 1:7. The coordinate system used in this study has its x-origin at the toe of the wave paddle and is defined positively towards the beach; the vertical z-origin is at the still water level (z=0) and is defined positively upwards. The rigid profile used here was the same profile as the one used in recent studies focusing on the hydrodynamics under breaking waves [22, 23].

The water surface elevation was measured by means of Resistive Wave Gauges (RWG, solid blue lines), Acoustic Wave Gauges (AWG, empty blue squares) and Pore Pressure Transducers (PPT, solid black squares). The WGs and PPTs were deployed at fixed positions along the flume. The AWGs were moved during the experimental campaign in order to increase the spatial resolution of the measurements. For most of the wave conditions the water surface elevations were measured at 32 different locations in total. All water surface information data were directly acquired by the wave paddle acquisition system at a sampling frequency of 40 Hz.

A mobile equipment carriage was used with a vertically moving frame from which several instruments could be deployed (Figure 2). This mobile frame ensured positioning with +/- 1 cm horizontal and +/- 1 mm vertical accuracy, and was instrumented with 2 ADVs (Nortek Vectrino), 6

OBSs and 1 PPT. The OBS on the frame had an equidistant spacing of 0.17 m in vertical direction, while the ADVs had a distance between them of 0.27 m. The lowest OBS and ADV on the frame had the same vertical positioning with a minimum distance to the bottom bed of 0.11 m. By repeating the same wave condition while varying the position of the mobile frame a good spatial discretisation along the wave breaking location (with a resolution of 0.5-0.25 m horizontally) has been obtained for both velocity and OBS measurements. Figure 1 shows the locations of the mobile frame (red dashed lines) during the experiments. The mobile frame was positioned at 12 different locations for the 3 conditions with the highest wave heights (H=0.7 and 0.8 m), and at 11 locations for all other tested conditions. For each test condition, at least 66 different OBS observations within the breaking area were collected.

The experimental procedure was as follows: 1) position the mobile frame at a pre-selected *x*-location; 2) position the frame vertically at the required *z* distance from the bottom (corresponding to the lowest OBS at 15 cm above the bed); 3) run the wave condition to be tested and check the acquired data (if data was erroneous the run would be repeated); 4) move the frame vertically to a higher *z* position (typically 8 to 9 cm higher) and repeat the same wave condition; 5) check the data before moving the trolley with frame to the new *x* and *z* position.

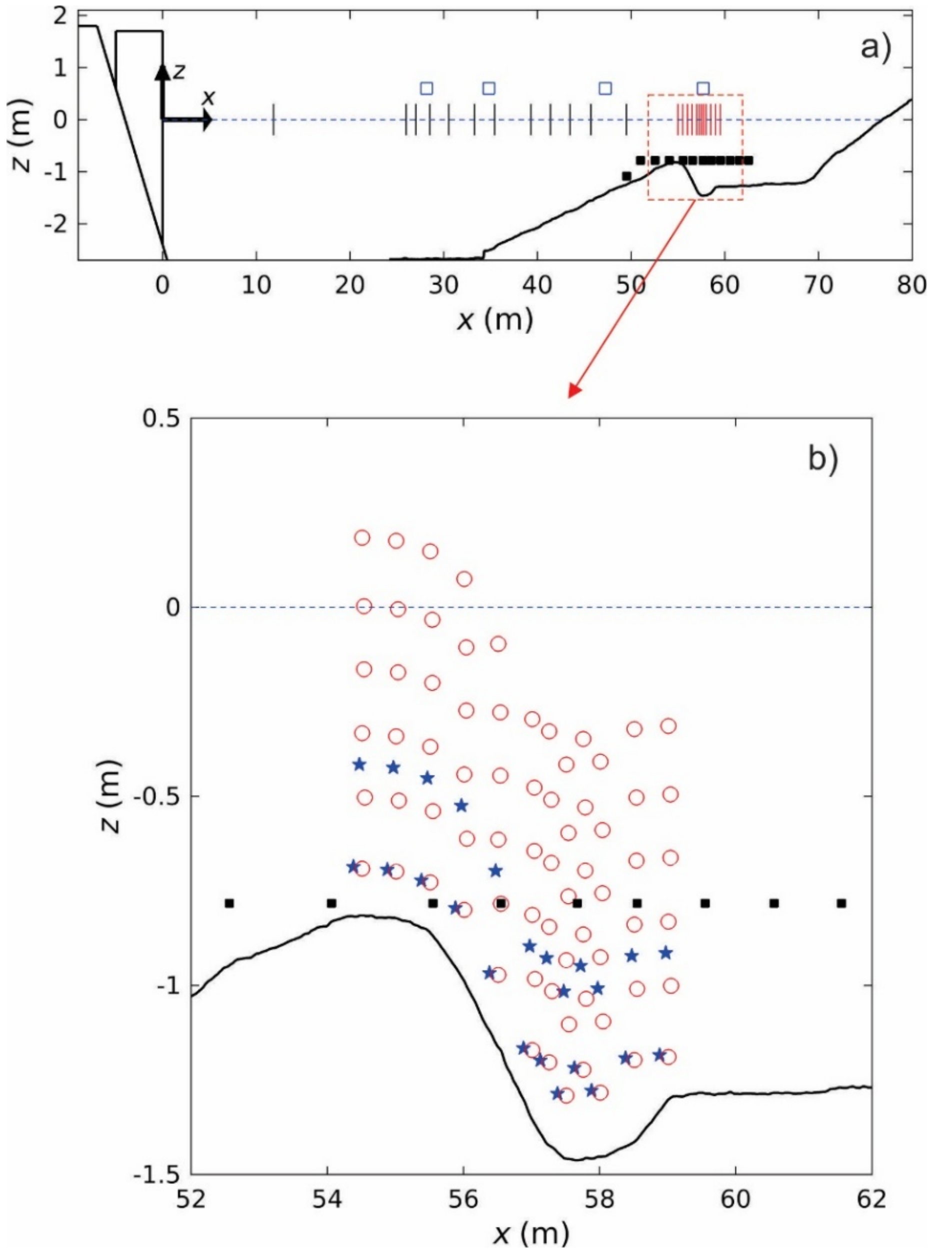

Figure 1. Experimental configuration: a) Bed profile including the location of water surface elevation measurements: Wave Gauges (solid black lines), Pore Pressure Transducers (solid black squares) and Acoustic Wave Gauges (empty blue squares). Red lines show the *x*-location of the mobile frame (Acoustic Doppler Velocimeters and Optical Backscatter Sensors). b) Close-up of bar and trough section where the measurement grid of OBS (open red circles) and ADV (blue pentagrams) are presented. The solid black squares indicate the pressure transducers on the wall of the flume (as in subplot a).

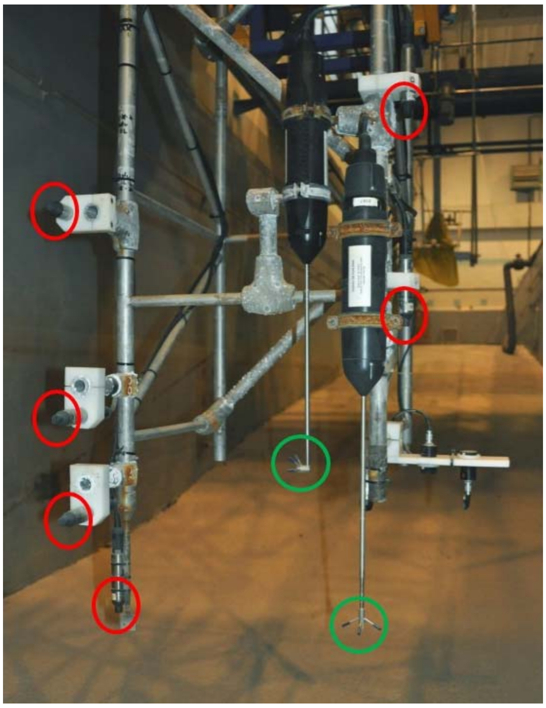

Figure 2. Close-up of measurement frame which was attached to the mobile carriage. The red circles show the OBSs and ADVs are encircled in green.

2.2 Wave conditions

The waves were generated by a wedge-type wave paddle based on first-order wave generation. No absorption system was used for these experiments, as using it would have limited the stroke of the wave paddle for larger wave height/period combinations. The tested waves were regular and included different types of wave breaking, ranging from waves that travel over the bar with minor breaking and just a slight decrease of wave height along the bar, to the most energetic wave condition with H=0.85 m and T=4 s, which produced a strong plunging breaker and air bubbles that reached the bottom of the flume. The present paper will focus only on those wave conditions that resulted in wave breaking on the bar. Table 1 shows the wave height and period of the test conditions, as well as the surf similarity parameter $\xi_0 = \tan\beta/\sqrt{H_0/L_0}$, where $\tan\beta$ is the offshore bar slope (1/12), L_0 is the deep-water wave length and H_0 is the deep-water wave height [24]. All test conditions were visually classified as plunging breaking. This classification is consistent with the predictive classification proposed by Smith and Kraus (1991) [25] for wave breaking characteristics at barred beach profiles, corresponding to tests with 5º and 10º offshore bar slope angles.

Each experimental run had a duration of 10 minutes, which was enough to produce a quasi-steady air bubble content produced by wave breaking at each location.

	H (m)	T (s)	ξ_0	H_0/L_0		H (m)	T (s)	ξ_0	H_0/L_0
M4_4	0.4	4	0.65	0.016	M5_6	0.5	6	1.02	0.007
M4_5	0.4	5	0.88	0.09	M6_3	0.6	3	0.39	0.047
M4_6	0.4	6	1.14	0.005	M6_4	0.6	4	0.53	0.024
M4_7	0.4	7	1.43	0.003	M6_5	0.6	5	0.72	0.013
M5_3	0.5	3	0.42	0.039	M7_3	0.7	3	0.36	0.055
M5_4	0.5	4	0.59	0.020	M7_4	0.7	4	0.49	0.028
M5_5	0.5	5	0.79	0.011	M85_4	0.85	4	0.45	0.034

Table 1. Information of tested wave conditions. Wave height (H); wave period (T); surf similarity parameter or Iribarren number (ξ_0); and offshore wave steepness (H_0/L_0).

2.3 Data processing

The water surface elevation was acquired by means of Resistive Wave Gauges, Acoustic Wave Gauges and Pore Pressure Transducers. The AWG data were despiked using a phase-space algorithm originally developed to despike ADV data in bubbly flows [26]. The Pore Pressure Transducers signal was converted to water surface elevation using linear wave theory (Tucker and Pitt 2001 [27] with the cut-off frequency obtained by Neumeier 2006 [28], 0.05-0.33 Hz). The ADV velocity data were despiked using the method developed by Goring and Nikora (2002) [29]. Low quality data, where signal-to-noise ratio and signal amplitude were below 15 and 75 dB respectively, were discarded. The ADV time series that produced a percentage of low quality data higher than 25% were discarded (the discarded data represented 16 time series out of 310 in total, i.e., 5%). Most of the discarded ADV time series had poor quality data due to the large number of air bubbles interfering with the ADV measurement positions, which occurred typically for the ADVs close to the water surface during the most energetic wave conditions.

For measurement locations around the crest of the bar, some OBS sensors were emerged during the trough phase of the waves. The OBS data reported in this paper are those that were completely submerged for more than 95% of the duration of the time series. In order to determine the submergence ratio of each OBS, its z-location was compared with the measured water surface elevation at each x OBS position.

In order to determine the threshold at which a peak will be considered as an air bubble event, several benchmark experiments were performed to measure the OBS background noise. These benchmark experiments included measurements in still water as well as measurements in the deeper section of the flume under non-breaking waves and, hence, in the absence of air bubbles. Three OBSs were used during these benchmark conditions and the noise level of the measurements, plus the standard deviation of that noise, exhibited a mean voltage value of 0.0064 V. The upper measurement limit of the OBS is at 4.8 V, and a value representing 2% of the upper limit was selected as a threshold signal for the OBS equipment to detect air bubbles. This value, which corresponds to a voltage of 0.096 V, is 15 times higher than the computed background noise, and is therefore considered to be high enough to assume that all OBS readings above this threshold will be produced by air bubbles. This assumption was verified through benchmark tests involving 30-minute time series in still water conditions and with non-breaking waves, in which no air bubble events (V above the 0.096 V threshold) were detected.

The OBS data are reported in volts, and the measured events will be used as a proxy for air bubbles. The light scatter measured by the OBS in the presence of air bubbles is controlled by the number as well as the size of the air bubbles. Consequently, the OBS voltages cannot be correlated to a physically meaningful variable such as void fraction or amount of bubbles. Similarly, it was decided not to convert the OBS voltages to Suspended Sediment Concentrations, because the transformation is dependent on the sediment characteristics and will therefore limit the applicability of the presented values.

At the start of a run there is a transient phase which lasts less than 3 minutes, in which the wave breaking location and wave breaking characteristics (including the water column air bubble content) are not stable [30, 31]. Therefore, for each 10 min run the first 3 minutes of data were discarded, and only the remaining 7 minutes of the time series were considered for further data analysis.

3.- Water surface elevation and velocities under tested conditions

Before looking into the air bubble distribution measurements, it is important to describe first the local hydrodynamics around the breaking location. Therefore, this section describes the wave breaking process, the undertow and compares the results to previous wave flume experiments with a barred profile.

All reported wave conditions produced wave breaking on top of the bar. Following a set of preliminary tests, the measurement area was chosen to be between 54.9 and 60 m, which ranges from the top of the bar crest up to 2 m shoreward of the bar trough. No wave absorption was activated during these tests in order to use the full stroke of the wave paddle, thus allowing the paddle's largest wave height/period combinations. Wave height measurement repeatability was studied from the 11 or 12 time series repeats of each condition (with the mobile frame at varying locations). The maximum standard deviation, considering all measurement positions and wave heights, was 0.05 m (for tests with H=0.7 and 0.85 m), while the mean standard deviation for each test condition, considering all the measurement points and repetitions performed, was 0.01 m. The excellent repeatability of the tested waves is shown in Figure 3, where the empty circles present the repeated tests measurements for the same wave conditions, and the solid circles represent the mean of the measured values.

Table 2 shows more detailed information about the wave breaking characteristics as well the location and magnitude of the maximum measured undertow velocity ($v_{\max}$), and the position at which this maximum undertow velocity was measured ($x_{v\max}$). The most energetic tested condition throughout these tests, M85_4 corresponding to H=0.85 m and T=4 s, was the same wave condition as that previously described by van der A. et al (2017) [22] for the same bottom profile. A detailed analysis of the hydrodynamic processes is beyond the scope of the present paper. The reader is referred to van der A et al. (2017) [22] and van der Zanden et al. (2018) [23] for a more detailed description of wave heights, velocity fields, and turbulence distributions for the most energetic breaking wave condition.

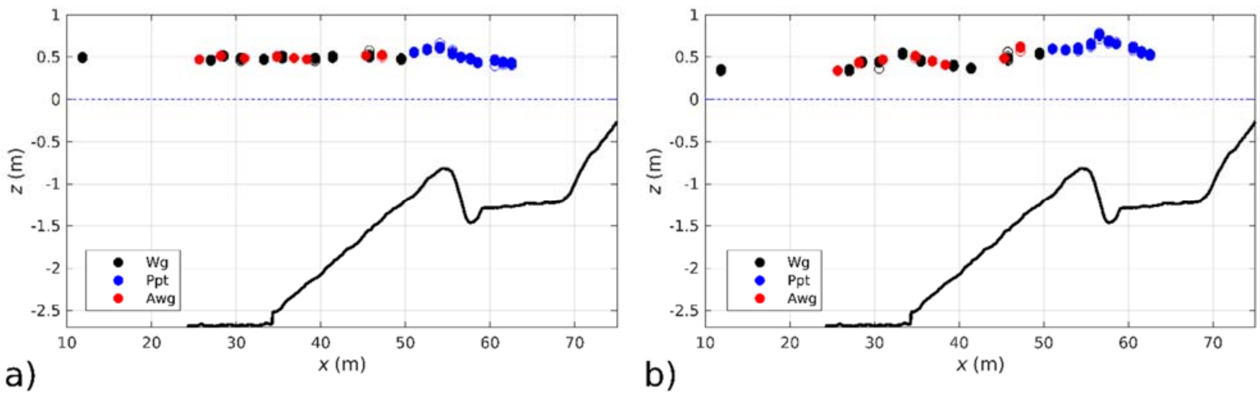

Figure 3. Time-averaged wave heights for 11 test repeats (open circles) and mean wave height over all repeats (filled circle), for wave condition M5_3 (a), and M4_7 (b).

Tested waves	H_b (m)	Ω_b	γ_b	h_b (m)	x_{imp} (m)	v_{max}(m/s)	$x_{v\ max}$ (m)
M4_4	0.44	1.09	0.46	0.95		0.15	57.88
M4_5	0.59	1.69	0.62	0.95	57.4	0.25	58.88
M4_6	0.71	2.37	0.63	1.14	57.6	0.22	58.88
M4_7	0.60	2.31	0.42	1.43		0.22	57.88
M5_3	0.45	0.82	0.54	0.83	57.6	0.19	57.88
M5_4	0.56	1.11	0.59	0.95	57.4	0.28	57.88
M5_5	0.74	1.69	0.78	0.95	57.0	0.42	58.38
M5_6	0.83	2.22	0.73	1.14		0.40	58.88
M6_3	0.53	0.81	0.64	0.83	56.8	0.39	57.88
M6_4	0.69	1.14	0.73	0.95	56.5	0.39	57.88
M6_5	0.85	1.62	0.90	0.95	55.6	0.47	56.88
M7_3	0.65	0.85	0.78	0.83	56.5	0.47	58.38
M7_4	0.81	1.14	0.86	0.95	56.1	0.43	57.63
M85_4	0.99	1.15	1.05	0.95	54.9	0.63	56.47

Table 2. Information on the tested wave conditions (targeted and measured across the study domain). Wave height at breaking (H_b); breaker height index (Ω_b, where $\Omega_b=H_b/H_0$); the absolute value of the water depth at breaking location (h_b); breaker depth index (γ_b computed as $\gamma_b=H_b/h_b$); impinging point location (x_{imp}, where the plunging jet hits the water surface); maximum measured undertow velocity (v_{max}) and position at which the maximum undertow was measured ($x_{v\ max}$).

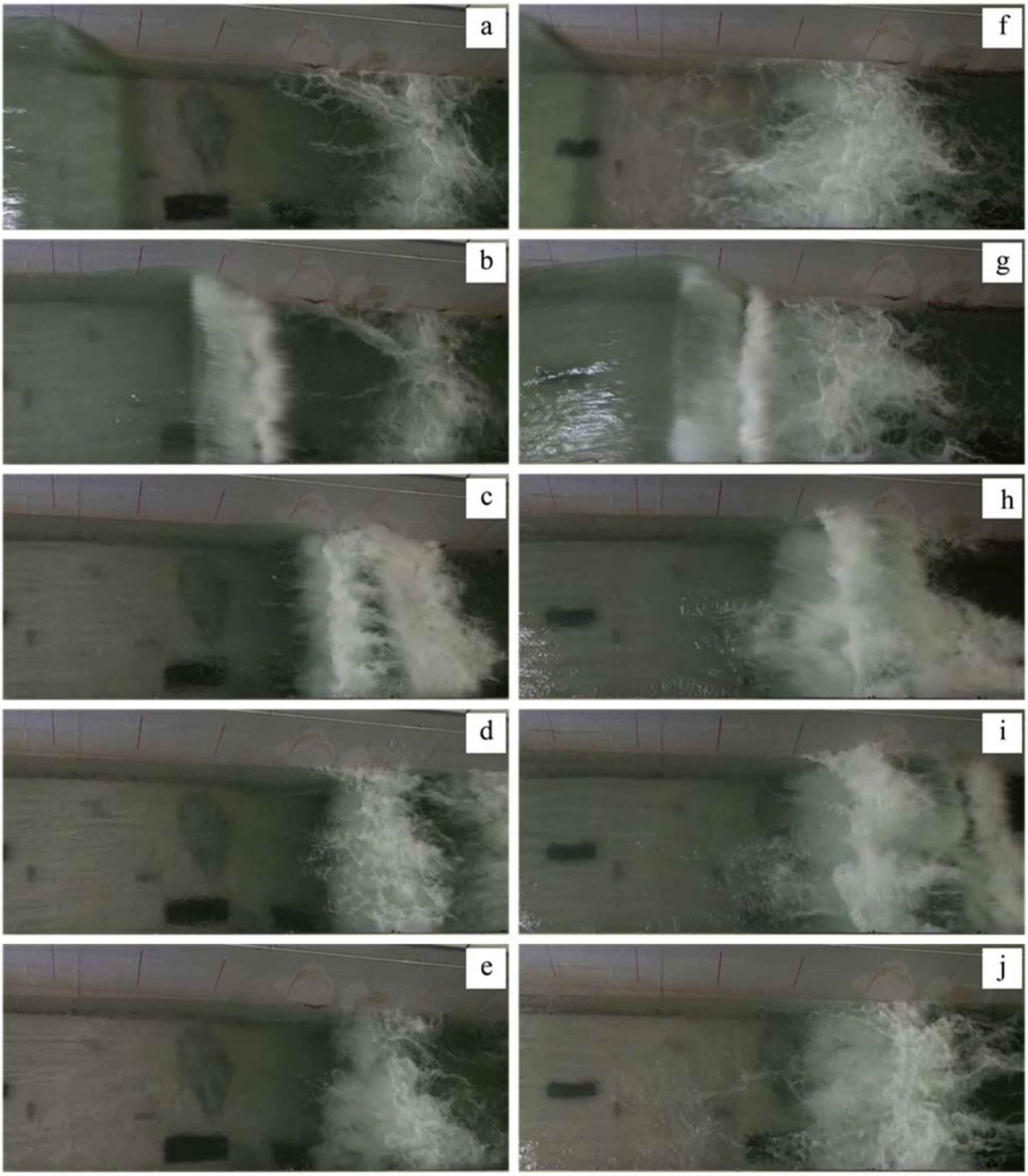

Figure 4. Images of the wave breaking sequence acquired from video recordings (left M7_4 and right M85_4).

The wave breaking process for M7_4 and M85_4 is illustrated through a series of images in Figure 4. The selected cases are among the most energetic tested waves, which produced high OBS voltage signals in the measurement area. The images correspond to different stages throughout the breaking process, starting at t/T=0 (4-a and 4-f) with the wave arrival on the left-hand side of each image. On the right-hand side of both images (4-a and 4-f), one can still see traces of air bubbles from the previous wave which are still trapped in the water column. The second frame of the sequence corresponds to *t/T*=0.15 (4-b and 4-g), the moment at which the plunging jet hits the water surface (the *x*-location of the impinging point is reported in Table 2). The next frames correspond to *t/T*=0.33 (4-c and 4-h) and show the final stage of the impinging jet penetrating the water column and creating a secondary wave. This wave propagates shoreward and, in the subsequent frames (*t/T* = 0.5, 4-d and 4-i), it can be seen leaving the field of view on the right hand side. Finally, the last images (4-e and 4-j) correspond to *t/T*=0.75 and show air bubbles still remaining in the water column as they emerge from the highly turbulent area.

The impinging positions in Table 2 were established using the video recording data. The images were studied frame by frame using the reference points on the wall of the flume (which has a mark for every meter) to determine the impinging positions. The blank spaces in Table 2 correspond to conditions for which the impinging point could not be accurately established, since it occurred outside the field of view of the fixed camera. Comparison of the impinging point and the location of the air bubbles showed that the maximum air bubble peak always occurs onshore of the impinging point and around the middle of the first splash roller (as previously also reported by Blenkinsopp and Chaplin 2007 [32] or Lim et al. 2015 [33]).

Undertow velocities were computed at all positions for each test, and the maximum undertow for each wave condition is shown in Table 2 ($v_{\max}$). Maximum undertow velocities occur between the trough of the bar and the bar crest, where the undertow negotiates the bar shape (Figure 5). The undertow velocities match previous measurements performed by van der A et al. (2017) [22] for the same profile and the same wave condition (M85_4). The differences between the van der A et al. (2017) [22] experiments and those reported here reside in the shorter duration of the present time series and the higher spatial and temporal distribution of velocity measurements performed by van der A et al. (2017) [22].

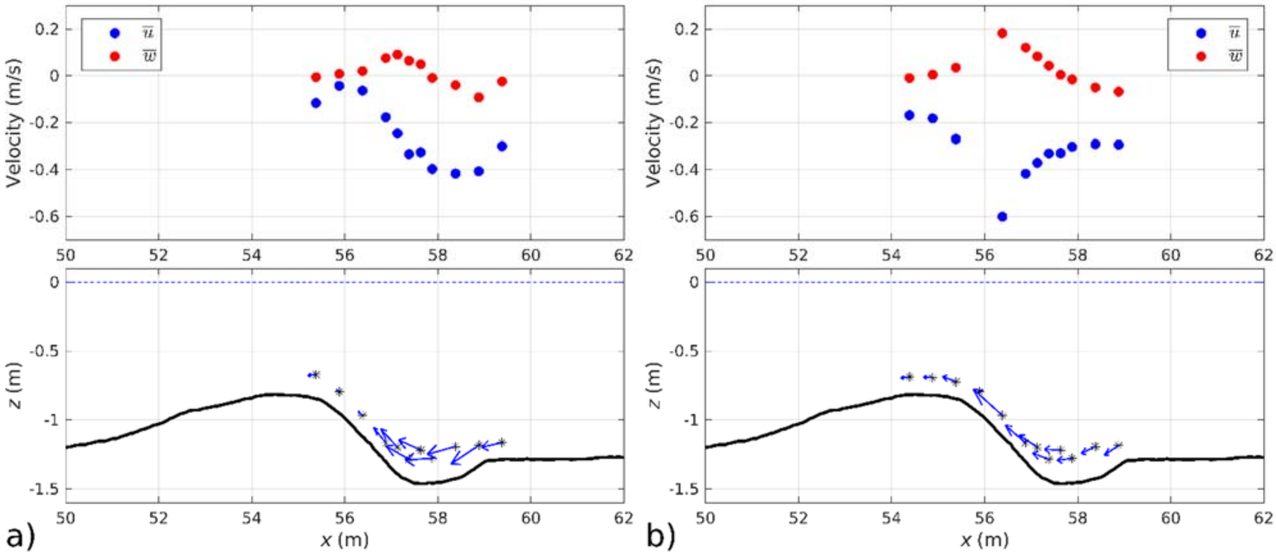

Figure 5. Cross-shore (blue) and vertical (red) mean velocities are shown in the upper panel while the lower panel contains the bathymetric profile with the black solid line. The measurement position is indicated by a black star and the magnitude of the measurement by means of the blue velocity vector. The velocity measurements were performed at a mean distance of 15 cm from the bottom. a) for M5_5 (*H*=0.5m and *T*=5s), and b) for M85_4 (*H*=0.85m and *T*=4s).

4.- Air bubble content induced by wave breaking

4.1 Air bubble measurements repeatability

Previous experiments illustrated the good repeatability of wave height and velocity measurements within the CIEM flume over mobile bed [34, 35] and fixed bed conditions [23]. In order to study the air bubble content repeatability, the present paper will study wave-by-wave OBS voltage repeatability for a monochromatic wave time series, as well as the repeatability of the OBS mean voltage for different runs of the same wave time series. Note that the OBSs measure the backscatter caused by air bubbles moving upwards due to buoyancy, but with a strongly 3D movement induced by the highly turbulent flow due to wave breaking [21]. Therefore, it is expected that OBS measurements present lower repeatability than water surface elevation and velocity measurements.

The wave-by-wave repeatability of air bubble measurements along a time series was evaluated considering the phase-average ensemble of each OBS time series. The zero-up crossing of the water surface at the most offshore pressure sensor was used to compute the phase-average times at each OBS. The OBS ensembles were time-referenced with these zero-up crossing points, in such a manner that t/T=0 corresponds to the zero-up crossing of the water surface. Figure 6 shows the ensemble-averaged of water surface elevation on the upper row, and the OBS signals on the following rows at three different *x*-locations for two different wave conditions (M6_4 and M85_4, both with a 4 s period). Results are presented here for the uppermost OBS, i.e. the one closest to the water surface, which is the sensor most exposed to bubbles. At this elevation, the number of events within the time series that measure air bubble peaks over the fixed threshold is significant (between 68-94% and 100% of waves produce voltage peaks over the threshold for M6_4 and M85_4 respectively). In addition, due to the larger turbulence close to the water surface, the air bubble events are strongly mixed, thus increasing the standard deviation (dashed cyan lines) of the events relative to the computed mean (black thick line) of the ensemble. There is a correlation between the air bubble distribution along the water column and the wave breaking induced turbulence, as previously shown by Mori et al. (2007) [12] or Lim et al. (2015) [33]. Another source of turbulence will come from the air bubbles entering and passing through the water volume, which inject and transfer energy into the flow, increasing the turbulent kinetic energy (TKE) production [33]. After comparing the air bubbles distribution with the TKE values computed by van der A. et al. (2017) [22] for M85_4, there is a correlation between larger TKE values and larger dispersion of peak events across the mean ensemble average (and with longer residence times of air bubbles within the water column).

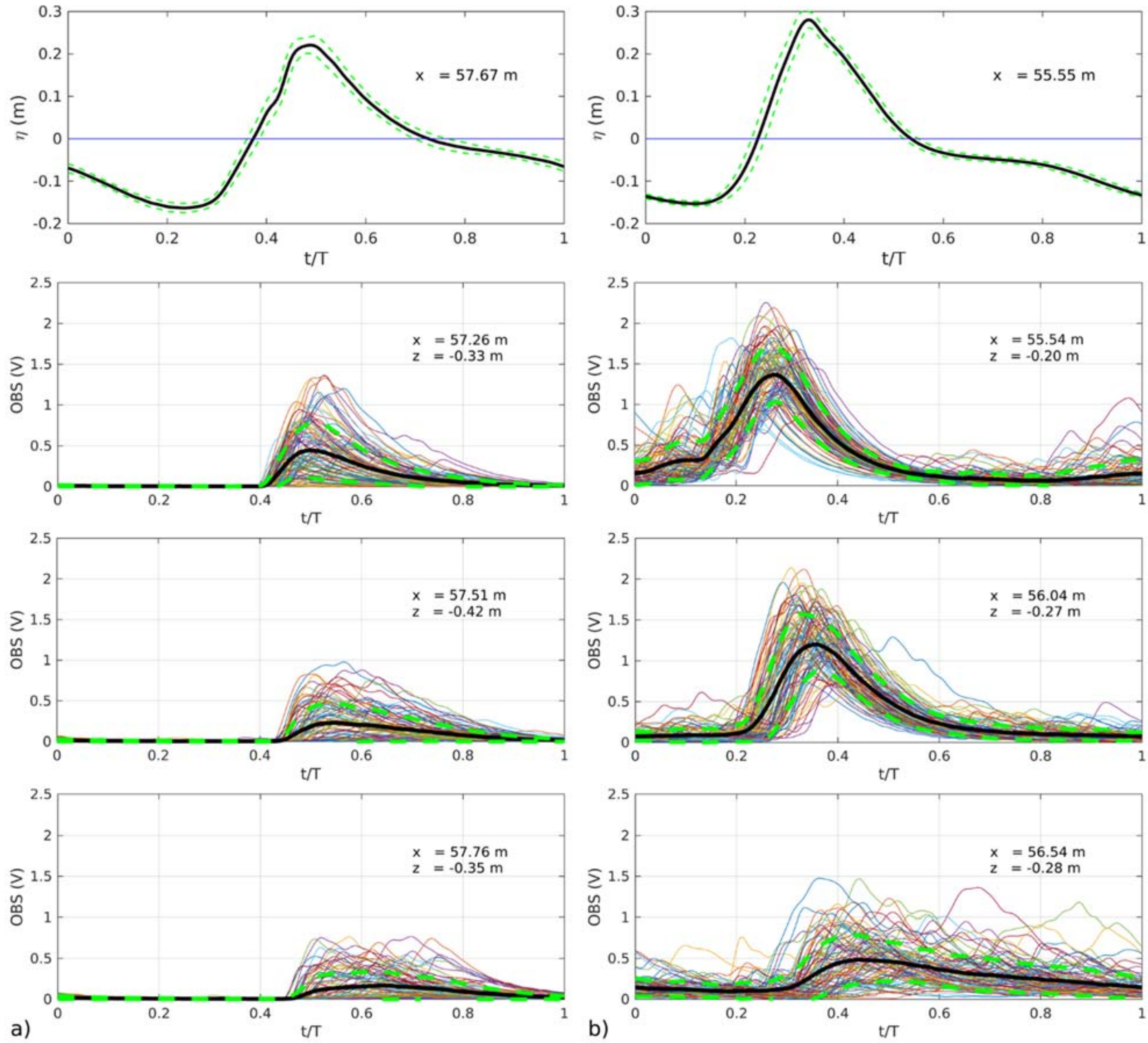

Figure 6. Phase-averaged water surface elevation (upper row) and OBS output (following rows) for different wave conditions: a) for *H*=0.6 m and *T*=4 s (M6_4), OBS at *x*=57.26, 57.51 and 57.76 m from top to bottom; b) for *H*=0.85 m and *T*=4 s (M85_4), OBS at *x*=55.54, 56.04 and 56.54 m from top to bottom. The black thick line shows the mean of the ensembles, while the dashed green lines indicate the standard deviation.

Table 3 quantifies the information presented in Figure 6, with P_{peaks} being the percentage of waves that produce air bubble events (an air bubble peak or event occurs when the OBS voltage exceeds the threshold of 0.096 V, i.e., P_{peaks} = 94% means that 94% of the arriving waves produce a voltage peak higher than 0.096 V). $\langle Oo_p \rangle$ is the mean of the OBS voltage of all peaks (where the angle brackets represent averaging over the entire time series). Std_p is the standard deviation of the measured peaks. Table 3 shows the OBS locations where the maximum voltages are measured as well as the next two shoreward OBS locations. The position with the highest voltage measurement correlates with the position with maximum P_{peaks} (*x*=57.26 m for M6_4 with P_{peaks}=94%, and *x*=55.54 m for M85_4 with

P_{peaks}=100%) and is always located after the impinging point of the breaking wave (cf. Table 2). In the M6_4 tested waves, there is a decrease in P_{peaks} while moving shoreward from the breaking position. Similarly, there is a decrease in $\langle Oo_{\text{p}} \rangle$ and Std_{p}. M85_4 presents a more energetic breaking condition, where a larger amount of air is entrained throughout the wave breaking process, thereby increasing the area in which air bubbles can be found and the duration of the air bubble events. All measured waves produce air bubble peaks at the three locations presented for M85_4, and the standard deviation relative to the computed mean values ($\langle Oo_{\text{p}} \rangle$) is lower than for M6_4. While it was close to 79% for M6_4, it is now 28% ($Std_p/\langle Oo_{\text{p}} \rangle$, on average over all studied locations). Despite significant differences in the air entrainment ratio induced by both wave breaking conditions (M6_4 and M85_4), there is a high repeatability of air bubble events after the breaking point with constant air entrainment at the same locations, low Std_{p} and constant repetition of the air bubble peaks within the wave phase.

	x (m)	P_{peaks} (%)	$\langle Oo_{\text{p}} \rangle$ (V)	Std_{p} (V)
M6_4 (H=0.6 m, T=4 s)	57.25	94	0.53	0.34
	57.50	68	0.30	0.25
	57.75	68	0.25	0.22
M85_4 (H=0.85 m, T=4 s)	55.50	100	1.49	0.30
	56.00	100	1.41	0.32
	56.50	100	0.68	0.28

Table 3. Computed air bubble OBS values. P_{peaks} indicates the percentage of waves that produce air bubble events (an air bubble event occurs when the OBS voltage goes beyond the threshold of 0.096 V), the mean of the measured peaks $\langle Oo_p \rangle$ and, lastly, the standard deviation of the measured peaks (Std_p).

The repeatability of air bubble events is now studied by repeating the times series of one wave condition. Table 4 presents the statistics of three considered parameters: time average OBS output in voltage $\langle Oo \rangle$, the percentage of waves that produce air bubble events P_{peaks}, and lastly the mean of the measured peaks over a time series $\langle Oo_p \rangle$. Due to time constraints, only one wave condition was repeated while the trolley was located around the area where most air bubbles could be seen. The percentage of differences (Eq. 1) is used to evaluate the repeatability of the acquired data. When considering the percentage difference for the time averaged OBS voltage ($\langle Oo \rangle$) for M85_4, the maximum difference between the various OBSs (each OBS presenting information for a different z location) is 23%, while the mean difference is 14%. The percentage difference for P_{peaks} has a maximum value of 20% and a mean value of 8%. Finally, the percentage difference for the mean concentration of peaks ($\langle Oo_{\mathrm{p}}\rangle$) has a maximum value of 14% and a mean value of 6%.

$$\text{Eq. 1} \quad \frac{|V_1 - V_2|}{\frac{(V_1+V_2)}{2}} \times 100 = Percentage\ difference$$

Test numbers and conditions	Obs	$\langle Oo\rangle$ (V)	P_{peaks} (%)	$\langle Oo_p\rangle$ (V)
M85_4 (H=0.85 m, T=4 s)	1 (-0.69 m)	0.016 // 0.015	26 // 23	0.08 // 0.08
	2 (-0.50 m)	0.048 // 0.060	58 // 71	0.26 // 0.30
	3 (-0.33 m)	0.146 // 0.150	99 // 99	0.78 // 0.77
	4 (-0.16 m)	0.464 // 0.369	100 // 100	1.60 // 1.49

Table 4. OBS voltage signal (as a proxy for air bubbles) acquired at x=55.5 m. Only the lower 4 OBSs are shown, i.e. those presenting a submergence ratio higher than 95% of the computed time. Red values for the first time the time series was run and black values for repetition. The grey value in brackets next to the OBS number denotes the submergence distance to still water level in m.

When comparing the obtained results of Table 4 and 3 it is evident that the variability of OBS measurements between repeats of the same test (Table 4) is lower than the variability of the measured parameters within the time series of one test repeat (Table 3). This implies that the statistics obtained over one test repeat are sufficiently converged.

4.2 Horizontal and vertical variability of air bubbles effects

After presenting the repeatability of the OBS for capturing air bubble events, Figures 7 and 8 show the spatial variation of the air bubble events for those test conditions that produced a larger distribution of OBS air bubble peaks (P_{obs}>30 %, where P_{obs} is the variable that denotes the percentage of OBSs that measure air bubble peaks). Figures 7 and 8 show a different wave condition for each row: the plots on the left show the mean of the V computed during the peaks measured at each location; and the plots on the right show the P_{peaks} to present the distribution of air bubble events across the study area. The red dashed line shows the minimum envelope of the wave troughs and the black dots show the wave height. The OBSs that have not been coloured (empty red circles) are those that were emerged for >5% of the time, and were therefore excluded from the present analysis.

Table 5 shows the summary of data collected from all test conditions. Note that the data of OBSs that were emerged more than 5% of the measurement time were discarded (empty red circles in

Figures 7 and 8), as well as the OBSs that showed voltage peaks for less than 10% of the waves (a low percentage of air bubble events was discarded in order to avoid outliers distorting the mean values). Table 5 shows two different types of variables: the first ones are local variables (white background) that show information averaged in time at a unique location within the grid of OBS measurements for each test condition, while the second ones are global variables (grey background) that present a double average (in time and space) in order to provide information of the complete study area. The local variables include: the maximum peak voltage measured along the measurement grid ($\langle Oo_p \rangle_{max}$); the penetration depth, $z_{p\ \mathrm{max}}$, indicating the absolute value of the maximum depth where the OBSs were able to measure air bubble peaks (OBS signal > 0.096 V) for more than 10% of waves; and the dimensionless variable obtained from the ratio between $z_{p\ \mathrm{max}}$ and H. The global variables include the percentage of OBSs that measure peaks (P_{obs}), and the temporally and spatially averaged OBS voltage $\overline{\langle Oo_p \rangle}$ where the overbar represents a spatial average. Therefore, the latter indicates the mean of the air bubbles peaks measured by the OBS in the study area.

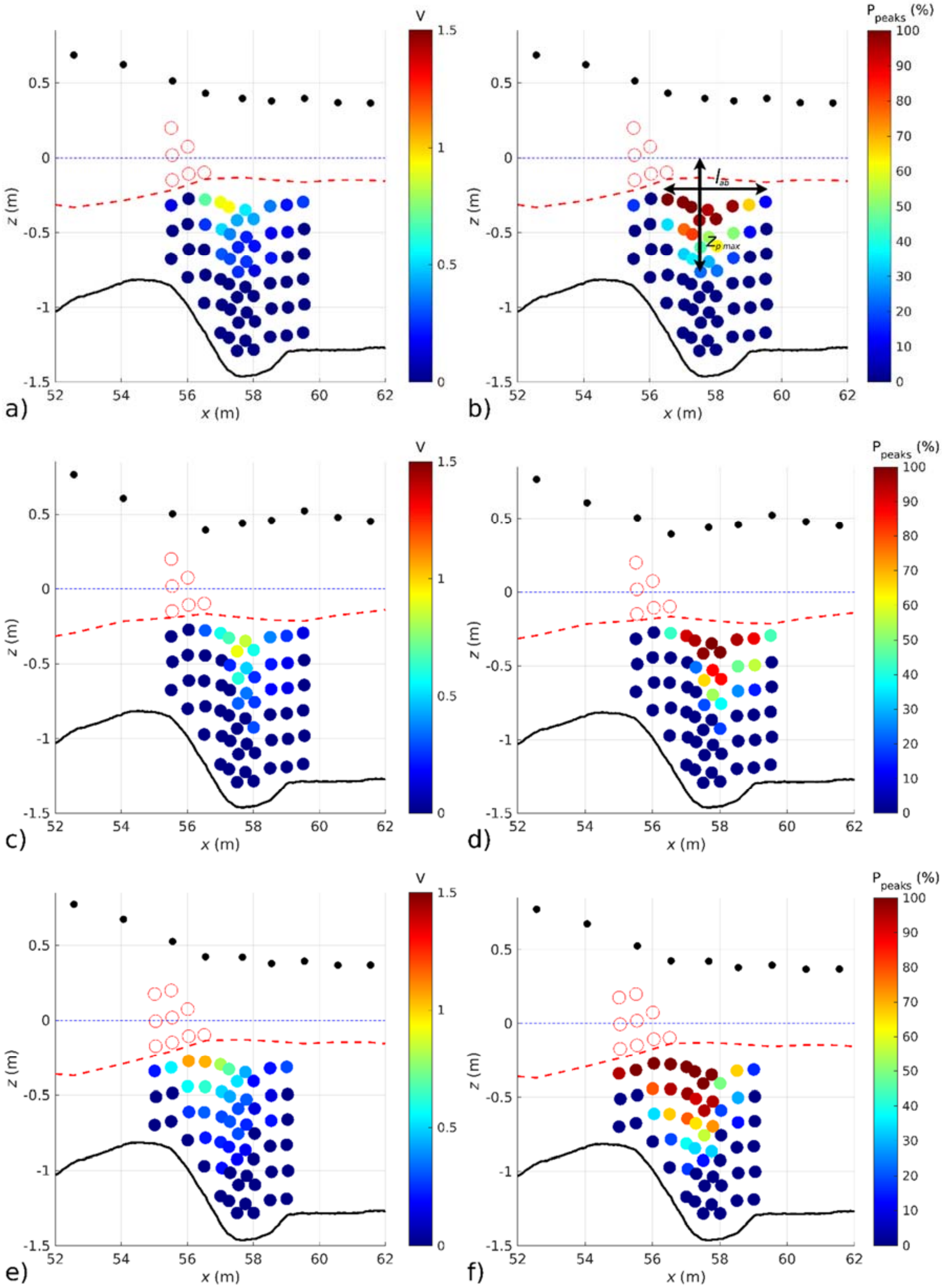

Figure 7. Optical backscatter measurements for M5_5, M5_6 and M6_5 waves from top to bottom respectively. The left-hand side panels (a, c and e) show the maximum voltage measured at each location. The right-hand side panels (b, d, e) show the percentage of waves producing a peak in OBS signal at each location. The solid black line shows the concrete bottom. The blue dashed line shows the still water level, the red dashed line the minimum of the wave troughs and the black dots the wave height.

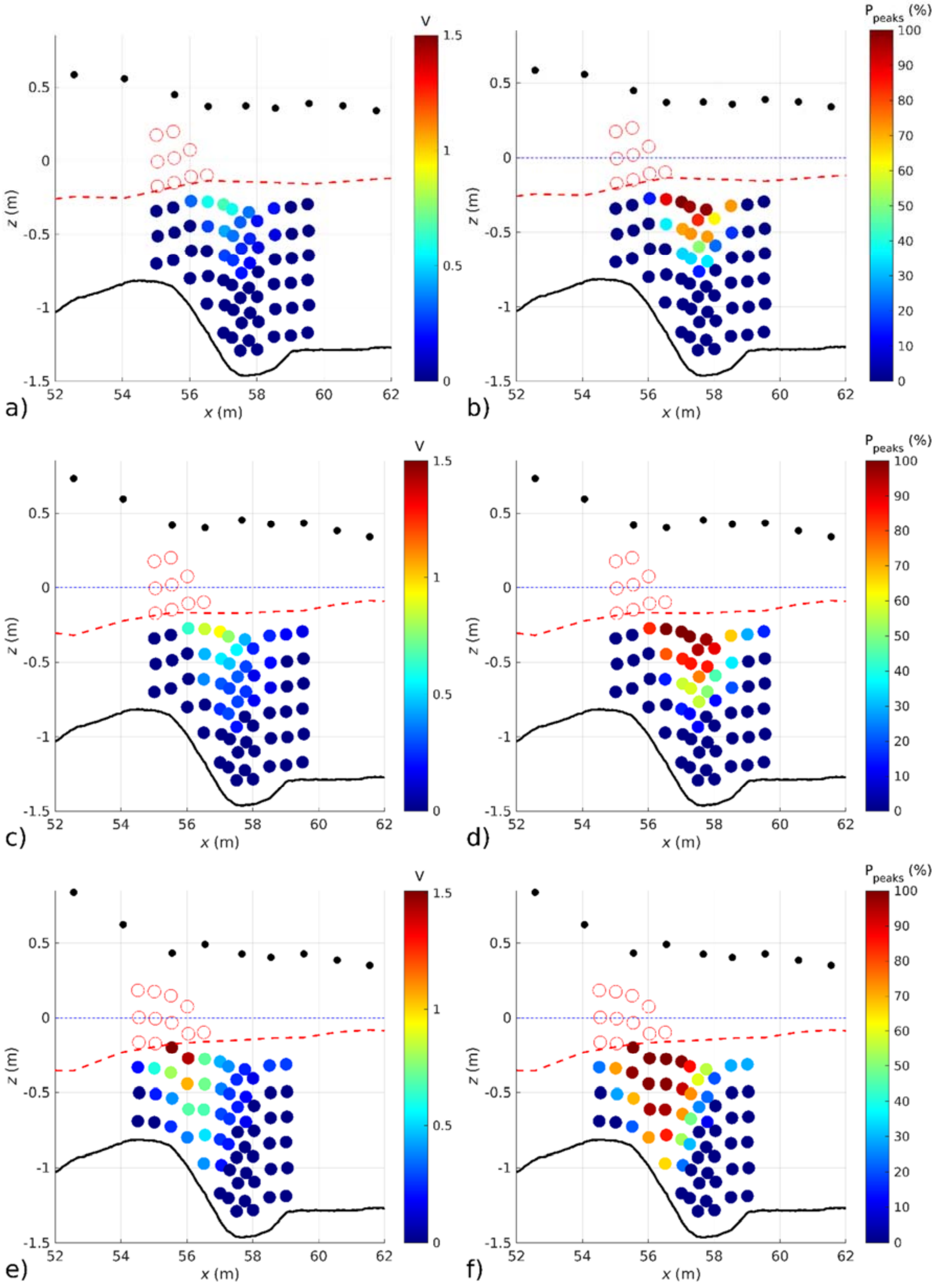

441 Figure 8. Optical backscatter measurements for M7_3, M7_4 and M85_4 waves from top to bottom respectively. The
442 left-hand side panels (a, c and e) show the maximum voltage measured at each location. The right-hand side panels (b,
443 d, e) show the percentage of waves producing a peak in OBS signal each location. The solid black line shows the
444 concrete bottom. The blue dashed line shows the still water level, the red dashed line the minimum of the wave troughs
445 and the black dots the wave height.

Tested waves	H_b (m)	$\langle Oo_n \rangle_{max}$ (V)	$z_{p\ max}$ (m)	$z_{p\ max}/H$	P_{obs}	$\overline{\langle Oo_n \rangle}$ (V)
M4_4 (*H*=0.4 m, *T*=4 s)	0.44	0.13	0.15	0.38	2 %	
M4_5 (*H*=0.4 m, T=5 s)	0.59	0.44	0.60	1.50	13 %	0.29
M4_6 (*H*=0.4 m, *T*=6 s)	0.71	0.32	0.41	1.03	8 %	
M4_6 (*H*=0.4 m, *T*=7 s)	0.60	0.21	0.41	1.03	8 %	
M5_3 (*H*=0.5 m, *T*=3 s)	0.45	0.15	0.41	0.82	2 %	
M5_4 (*H*=0.5 m, *T*=4 s)	0.56	0.21	0.42	0.84	7 %	
M5_5 (*H*=0.5 m, *T*=5 s)	0.74	0.93	0.76	1.52	40 %	0.35
M5_6 (*H*=0.5 m, *T*=6 s)	0.83	0.91	0.92	1.84	35 %	0.39
M6_3 (*H*=0.6 m, *T*=3 s)	0.53	0.32	0.59	0.98	12 %	0.22
M6_4 (*H*=0.6 m, *T*=4 s)	0.69	0.53	0.70	1.17	28 %	0.29
M6_5 (*H*=0.6 m, *T*=5 s)	0.85	1.07	0.98	1.63	56 %	0.38
M7_3 (*H*=0.7 m, *T*=3 s)	0.65	0.66	0.76	1.09	31 %	0.32
M7_4 (*H*=0.7 m, *T*=4 s)	0.81	0.94	0.93	1.33	45 %	0.38
M85_4 (*H*=0.85 m, *T*=4 s)	0.99	1.49	0.98	1.15	55 %	0.48

Table 5. Measured wave height and air bubble content information for all tested conditions: Wave height at breaking (H_b); maximum of the $\langle Oo_p \rangle$ values computed along the measurement grid ($\langle Oo_p \rangle_{max}$); the maximum penetration depth ($z_{p\ max}$) is computed as the absolute value of the maximum depth where the OBSs measure air bubbles for more than 10% of the waves; relative penetration depth as ratio of $z_{p\ max}$ and H; percentage of OBSs that present peaks over the 0.096 V threshold (P_{obs}); and the mean value of the voltage peaks over all OBS locations ($\overline{\langle Oo_p \rangle}$).

P_{obs} also provides information of the distribution of air bubbles across the study area. All tests in Table 5 report air bubble events around the impinging point. Even the two cases that present a lower number of OBSs measuring air bubble events, P_{obs}=2 %, which represent a single OBS measuring air bubble events, have values of 0.13 and 0.15 V as mean of the computed peaks for that OBS voltage. These measurements represent values around 1.4 g/l when converted to Suspended Sediment Concentrations (OBSs calibrated with d_{50}=0.25 mm sediment from the CIEM wave flume). Even if the peaks are local and do not appear constantly in the time signal, their values would be significantly high to distort Suspended Sediment Flux computations over the water column. For six out of the 14 tests in Table 5 the air bubble events occurred at more than 30% of the OBS measurement locations (P_{obs}>30 %). These tests, where air bubble events are more spread out across the study area, exhibit larger V values (as a proxy for air bubbles) and a larger percentage of waves producing air bubble events. These tests provide the most reliable data for the study of penetration depth and bubble length distribution, for comparison with previous data sets.

An important parameter to assess the air bubble impact in OBS locations is the penetration depth of air bubbles. Table 5 shows the penetration depth, $z_{p\ \max}$, defined as the absolute value of the maximum depth where the OBSs measure air bubbles for more than 10% of the waves (plotted in Figure 7-b). The air bubbles were seen to reach the bottom of the flume in the trough area (x=58 m) for the most energetic tested condition (H=0.85 m and T=4 s), so it is expected that the air bubbles would have reached larger $z_{p\ \max}$ if the bar trough had been deeper. The average penetration depth over all tests was 1.16H_0 (with a standard deviation value of 0.38H_0). The maximum penetration depth was 1.84H_0 for test condition M5_6, while the minimum penetration depth was 0.38H_0 for condition M4_4. When considering only those wave conditions that show OBS peaks for more than 30% of the measuring points, the mean penetration depth increases up to 1.43H_0 (with a standard deviation value of 0.29H_0). These measured values are in range with previous small scale experiments that exhibit penetration depths from 0.5H_0 [36, 33] to values of up to 2.4H_0 in Blenkinsopp and Chaplin (2007) [32].

The bubble cloud length, l_{ab}, indicates the longitudinal distance over which OBSs measure air bubble peaks for more than 10% of the arriving waves (as presented in Figure 7-b). Table 6 reports the length of air bubble clouds and the bubble area entrapped along the breaking area. The data presented show the characteristics of the larger events (P_{obs}>30 %) as these are cases that produce larger air bubble events and are therefore more easily captured by OBSs. The air bubble area (A_{ab}) is defined as the area where the air bubbles are measured between the maximum penetration depth and the wave trough. The lengths and area of the air bubbles shown in the table could have been larger for some cases if the measurement grid had been extended. The columns x_{init} and x_{end} report the information relating to the beginning and end of the air bubble plume. The information in brackets after x_{init} and x_{end} shows that P_{peaks} values at these positions were greater than 10% (in brackets the P_{peaks} values). The collected bubble distribution length l_{ab} has an average value of 0.12L_0. This value is in the same region as previous small-scale laboratory observations. For instance, Lim et al. (2015) [33], reported a bubble cloud length between 0.1L_0 and 0.7L_0. According to Kalvoda et al. (2003) [11], the maximum cloud lengths at the top and side view are 0.1L_0 and 0.16L_0 respectively.

Tested waves	l_{ab} *(m)*	x_{init}	x_{end}	A_{ab} *(m^2)*	max *t/T*
M5_5 (*H*=0.5 m, *T*=5 s)	2.97	56.54	59.51 (12%)	3.41	0.37
M5_6 (*H*=0.5 m, *T*=6 s)	2.97	56.54	59.51 (44%)	3.01	0.30
M6_5 (*H*=0.6 m, *T*=5 s)	4	55.01 (94%)	59.01 (16%)	3.58	0.57
M7_3 (*H*=0.7 m, *T*=3 s)	2.47	56.04	58.51	2.56	0.52
M7_4 (*H*=0.7 m, *T*=4 s)	3.47	56.04	59.51 (16%)	3.51	0.47
M85_4 (*H*=0.85 m, *T*=4 s)	4.5	54.51 (24%)	59.01 (29%)	3.88	1

Table 6. Main parameters of air bubble plumes. Length of the air bubble plumes measured in the upper layer of OBS and bubble area computed considering the bubble penetration depth and the wave trough. Max *t/T* indicates the maximum duration of the OBS ensemble average signal measuring over the V threshold, reporting the maximum duration of the air bubble events over the OBS grid.

Previous laboratory experiments described by Kalvoda et al. (2003) [11] presented maximum air bubble duration between 0.25*T* and 0.5*T*. Similarly, Lamarre (1993) [17] reported experimental data where the bubble duration expands up to 0.5*T* and where the plume is very compact with high void-fraction concentrations and a subsequent void-fraction decrease. Table 6 shows the maximum duration of air bubbles presence *t/T* measured during the present experiments. These data have been computed by considering the time that the OBS mean ensemble signal exceeds the settled voltage threshold. Within the presented large-scale data, which includes plunging breaking waves with wave heights significantly larger than previously presented small-scale data sets and, therefore, larger penetrations depths, the concentration of air bubbles within the time phase will largely depend on the depth of the measurement probe and its position from the impinging point. For OBS locations closer to the water surface, comparable to previous experimental data, and close to the impinging point, the air bubbles produce OBS measurements beyond the settled threshold with maximum spans that go up to 0.57*T*. The exception to this behaviour is obtained for the most energetic tested case (M85_4), where OBSs retrieve voltage signals over 0.75*T* at several positions and at one position, the signal exceeds the threshold during the entire wave period. For the latter case, the ensemble-averaged OBS signal can be seen in the lower panel of Figure 6-b. While this signal does not produce the largest peaks in OBS measurements, it exhibits the longest air bubble residence times. Note that this location, above bar trough, is also characterized by maximum TKE values [22], which may contribute to vertical mixing of air bubbles and contribute to the high bubble residence times. These values are also corroborated by the images presented in Figure 4. Panel f in Figure 4 (*t/T*=0) shows the new wave arriving on the left-hand side of the image, and the residual bubbly area at the right of the image (trough of the bar) presents a significant area where the air bubbles from previous waves are present in a highly turbulent flow.

Despite the good agreement of penetration depth and bubbles cloud length when compared to previous studies, there are other parameters and formulations in literature that our experimental data do not follow so closely. Hwung et al. (1992) [37] performed a set of small-scale experiments with a planar 1/15 slope measuring the air bubbles mixing in the surf zone, and provided a formula to describe the vertical distribution of their concentration during the breaking process. Following this formulation, the concentration of air bubbles hyperbolically decreases with water depth. Figure 9 shows a clear deviation of the hyperbolic function predicted by Hwung et al. (1992) [37] (Figure 9 is comparable to Figure 5 in Hwung's paper) at most of the studied locations. The deviation is sharper in cases where significant amounts of air bubbles were found (x from 56 to 57 m), where the voltage decreases linearly or keeps constant along the first meter of water column matching the wave breaking impinging jet which produces a periodic vortex at this location. The authors have observed that for low air bubble concentration and low penetration depths, there is a hyperbolic distribution of air bubbles along the water column, but there is also a clear deviation for larger air bubble concentration and larger penetration depths. The disagreement with the hyperbolic profile predicted by Hwung et al. (1992) [37] does not come just from the linear or constant distribution of the bubbles on the turbulent areas, but also from the narrowly located distribution of our air bubbles. In our case, the air bubble events and distribution are found between $0.08<x_b/L_0<0.26$, while the data reported by Hwung et al. (1992) [37] measure air bubble events between $0.34< x_b/L_0<0.79$ (where x_b is the distance from the breaking point position). These differences can be due to different sources, but here they have been attributed to three main causes: i) the small scale of the experiments presented by Hwung et al. (1992) [37] with H=6.11 cm and T=1.29 s; ii) the difference in bed slope (planar slope in Hwung et al. (1992) [37] experiments vs. the barred beach profile used in the present experiments); iii) the more accurate/sensitive equipment used by Hwung et al. (1992) [37] to measure the air bubbles (He-Ne Laser). The three above-mentioned parameters are relevant and can significantly affect the measurement of air bubble content (area and penetration depth) along the water column after breaking.

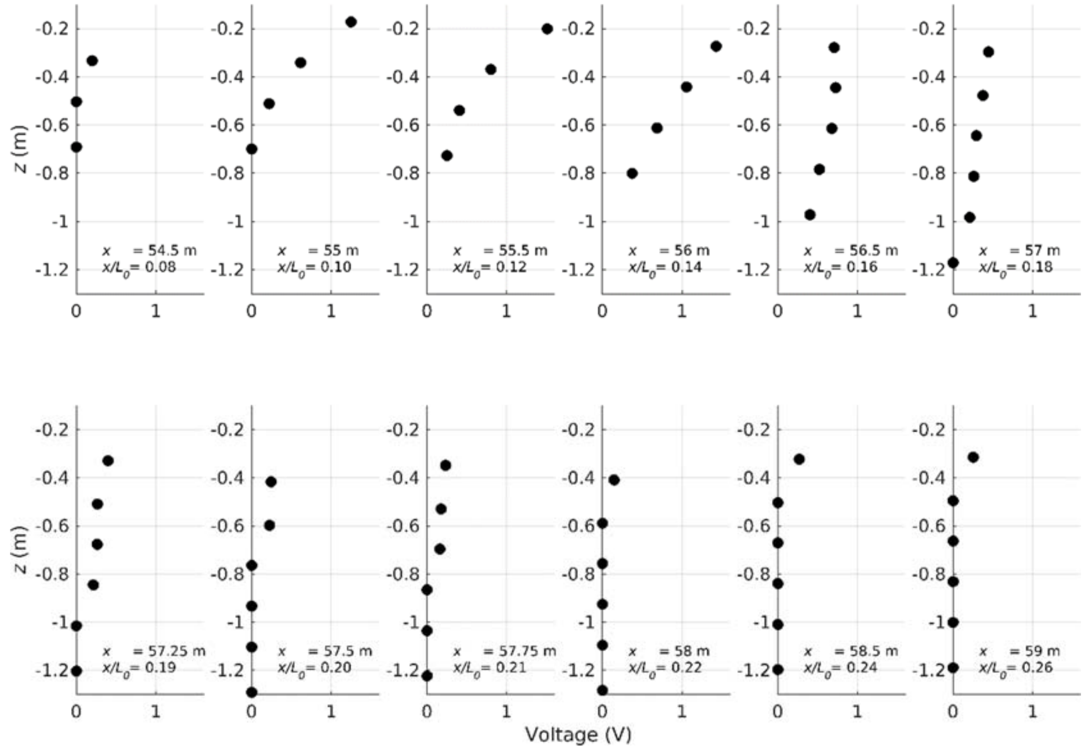

Figure 9. Time-averaged voltage over water depth for wave condition M85_4 (H=0.85 m and T=4 s).

5.- Discussion

The results presented here indicate that OBSs are sensitive to air bubbles. The presented data show that air bubble events collected by the OBS are phase-coherent and highly repetitive. The observations of bubble cloud length and penetration depth through OBSs are consistent with previous studies that used other instrumentation.

The use of a large-scale wave flume in this paper provides larger air bubble residence time and more homogeneous vertical air bubble distribution for breaking waves, in contrast to previous small-scale studies. However, the measured air bubble penetration depth and horizontal length distribution agree well with previous studies. This suggests that OBS equipment is less sensitive to air bubbles than previous equipment designed to measure void fraction and air bubble size.

While previous experiments have presented central air bubble distributions from the impinging point at deep water wave breaking conditions [32, 18], the data in this paper show a distribution of the air bubbles which has its centre shoreward from the impinging point. The beginning of the air bubble events from the impinging point is on average 0.4 m (from Tables 4 and 5), and most wave conditions exhibit limited air bubble events before the impinging point.

The highest value of the mean of measured peaks ($\overline{\langle Oo_p \rangle}$ = 0.48 V) and the maximum ($\langle Oo_p \rangle_{\max}$

= 1.49 V) of these peaks correspond to the most energetic test condition M85_4. OBS voltage measurements of 0.48 V and 1.49 V correspond respectively to sediment concentrations of 5 and 16 g/l when calibrated for a typical medium sand with d_{50}=0.25 mm. Such concentration values are of the same order of magnitude as suspended sediment concentrations measured close to the bed in the breaking region (5 to 7 g/l are typical values of suspended sediment concentration events free of air bubbles).

Although these extreme values correspond to the most energetic test condition M85_4, nevertheless the values reported in Table 5 tell us to be very cautious when interpreting OBS data collected in bubbly areas. When considering the tests for which P_{obs}>30%, the mean of the computed measured peaks at all stations is 0.38 V. This mean estimation can be done when considering just one location for each wave condition ($\langle Oo_p \rangle_{\max}$), obtaining a mean value of 1.0 V. Both values of 0.38 and 1.0 V correspond, for a d_{50}=0.25 mm sediment, to 4.0 and 10.6 g/l respectively, which is sufficiently high to induce a significant overestimation of the suspended sediment concentration and flux in surf zone conditions.

Different parameters have been studied to forecast the air bubble distribution across the surf zone. The focus is on predicting what breaking wave conditions will produce false OBS suspended sediment readings, which will help to better locate the measurement equipment across the surf zone in further experiments. Based on the correlations studied, the breaker depth index (γ_b=H_b/h_b) appears to be the best parameter to predict the spatial air bubble distribution (represented in dimensionless forms of $z_{p\ \max}$ and l_{ab}, computed by means of $z_{p\ \max}/h_b$ and $l_{ab}/T\sqrt{gh}$). Figure 10-a correlates the breaker depth index with the dimensionless penetration depth, which can be used to develop a predictive formula that can help users to determine the area where air bubbles will be found. The collected data were fitted to a first degree polynomial equation (Equation 2) with a coefficient of determination (R^2) equal to 0.89, which is plotted in Figure 10-b. The only data that were excluded to produce such a polynomial equation is the data from the most energetic case (M85_4, red dot in Figure 10-a), where the air bubbles were observed to reach the bottom of the profile and where therefore depth-limited.

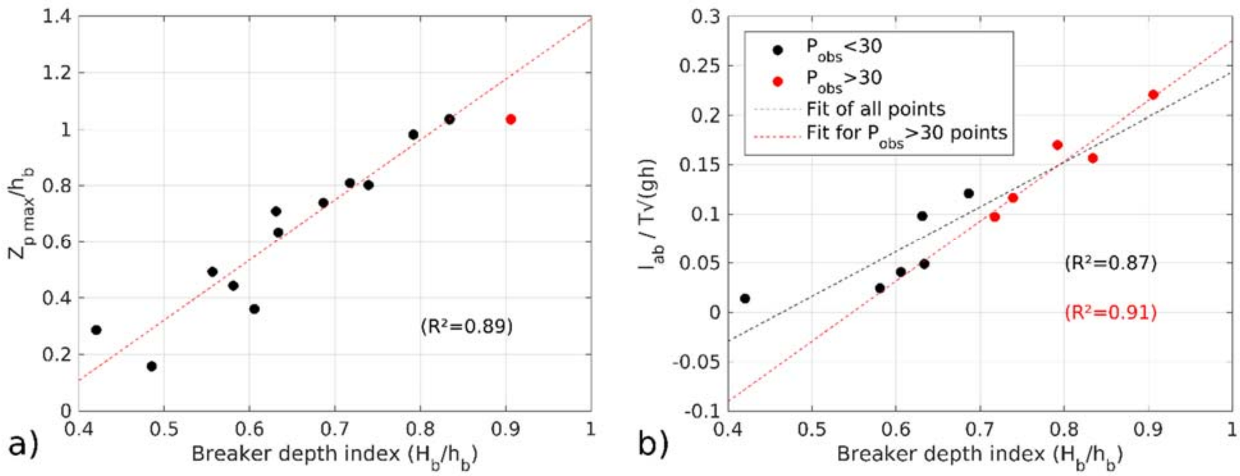

Figure 10. Correlations between breaker depth index and: a) Penetration depth, and b) the air bubble length.

Eq. 2 $\quad Z_{\mathrm{p\,max}}/h_b = 2.135\,\gamma_{\mathrm{b}} - 0.745 \quad (R^2 = 0.89)$

The second applicable formulation derived from the present results is obtained from the information shown in Figure 10-b. This panel presents the dimensionless air bubble cloud length ($l_{ab}/T\sqrt{gh}$) for all tests as a function of the breaker depth index (with h being the absolute water depth value at the toe of the wave paddle, 2.65 m). The black solid dots show the tests with small air bubble distribution (P_{obs}<30 %), while the red dots show the tests that have a larger distribution of air bubbles (P_{obs}>30 %). The black dashed line indicates the polynomial curve fit to all measured points (Equation 3) with its coefficient of determination (R^2=0.87). The red dashed line presents the polynomial curve fit (Equation 4) of the red dots (R^2=0.91), which from the authors' viewpoint is more representative of the air bubble distribution when considering the equipment and spatial resolution of the measurements.

Eq. 3 $\quad l_{ab}/T\sqrt{gh} = 0.45\,\gamma_{\mathrm{b}} - 0.21 \quad (R^2 = 0.87)$

Eq. 4 $\quad l_{ab}/T\sqrt{gh} = 0.61\,\gamma_{\mathrm{b}} - 0.33 \quad (R^2 = 0.91)$

The data here presented have been acquired using fresh water, and although there is some discussion on the effects of fresh versus salt water on the size and number of air bubbles under breaking wave conditions, there is a general agreement that, under salt water conditions, there is a large number of bubbles with a smaller size. Cartmill and Su (1993) [38] conducted a set of laboratory experiments to study the size and density of air bubbles for breaking waves using both fresh and salt water. Wave groups were generated in order to produce wave breaking and bubble plumes that were comparable in scale to moderate ocean waves. They reported differences in bubble size under salt and fresh water conditions, with the former ones being finer. The smaller size of bubbles in salt water was attributed to the coalescence of micro-bubbles in fresh water, which is inhibited by ionic repulsion of salt water (fresh water air bubbles join together more easily than in salt water conditions, where the ionic charges on the air bubbles' surface repel other air bubbles, thus preventing them from merging). Puleo et al. (2006) [10] also noted that in salty environments where bubbles tend to be smaller, OBS voltages are larger than the readings obtained using fresh water. Lastly, Anguelova and Huq (2018) [39] achieved similar results, reporting an increase in the number, with smaller size, of air bubbles induced by a salinity increase in the water. This effect was also attributed to the fact that air bubbles tend to shatter easily and do not join again under salt water conditions. Other authors, including Wu (2000) [40], claim that air bubbles in salty conditions are not smaller than in fresh water, but simply that more bubbles are entrained and produced in salt water conditions. According to Wu (2000) [40], the breaking process appears to be more important than bubble coalescence or shattering when considering the number and size of air bubbles.

6.- Conclusions

A laboratory data set was collected in a large-scale wave flume with the objective of quantifying spurious Optical Backscatter Sensor measurements produced by the presence of air bubbles. The analysis has spanned different depths and locations relative to the breaking point for plunging breaking waves over a fixed barred bed profile. Six OBS sensors were located on a mobile trolley that was moved along the breaking area while repeating 14 selected wave conditions that produced breaking waves over the barred profile. Water surface elevation was measured using Wave Gauges, Acoustic Wave Gauges, Pore Pressure Transducers and velocity measurements were made using Acoustic Doppler Velocimeters.

The OBS acquired data were processed after verifying that, in the absence of suspended sediment particles, the voltage peaks of the OBS sensors were produced by air bubbles. The experimental data presented confirm that the large amount of air bubbles produced at the wave breaking area have a significant impact on the OBS signal. The measured OBS voltages are consistent and repeatable for air bubble events across the entire measurement area. Formulations for air bubble penetration depth and bubble cloud length, obtained using small-scale experiments and air bubbles measurement equipment, were used to compare the acquired data. The result of this comparison was that the measured characteristics of the air bubbles (penetration depth and air bubble cloud length after breaking), collected under large-scale wave conditions and using OBS, lie within the range of previous studies that measured air bubbles and void fraction. On the other hand, the large scale experimental data set presents larger residence times of air bubbles in the water column and a more homogeneous air bubble distribution after the impinging point. Considering previous information, and the lower sensitivity of OBS to measure air bubbles than other equipment, the use of large scale facilities is recommended in further studies.

The data shows that under energetic wave conditions air bubbles can produce false suspended sediment concentrations even when deployed close to the bottom. The maximum mean average value obtained in the time series presented is 0.48 V, while the maximum mean of the peaks measured at the same location reports a value of 1.49 V. This represents 31% of the measurement range of the OBS (the calibration range of this OBS was up to a maximum of 80 g/l using a sediment with d_{50}=0.25 mm, with 0.48V corresponding to values of 5 g/l, and 1.49 V to 16 g/l). Such false readings are in the order of magnitude of previous suspended sand concentration measurements in surf zone conditions in the absence of air bubbles (mean values of 5 to 7 g/l). The area in which the air bubbles will affect OBS measurements is limited in space to the proximity of the impinging point, with a maximum longitudinal distribution length of 4.5 m and a maximum vertical penetration depth of 0.98 m in the present data set.

When large air volumes enter the water column and achieve significant penetration depths, the air bubble distribution differs from the hyperbolic vertical distribution observed by Hwung et al. (1992) [37]. The data presented show a linear correlation between the breaker depth index and: i) the measurements by the OBSs; ii) the air bubble penetration depth; and iii) the length of the air bubble cloud spreading at the surface. A linear correlation (Eq. 2 with R^2=0.89) was obtained to predict the dimensionless penetration depth as a function of the breaker depth index, while correlations on Eq. 3 and 4 have been obtained to predict the dimensionless air bubble cloud length as a function of the breaker depth index. These formulations will help to predict the water depth and distance from the breaking location at which the air bubbles can interfere with OBS measurements for wave breaking at barred beach profiles, offering a guideline for OBS usage in the surf zone.

Acknowledgements

We offer our gratitude to the CIEM staff, especially to Joaquim Sospedra for his endurance and leadership. The work described in this paper was supported by the European Community's Horizon 2020 Programme by means of the Hydralab+ Project (contract number 654110). This paper contributes to the Hydralab+ legacy together with a set of coordinated papers in other journals. Finally we acknowledge the economical funding and support received by the Secretaria d´Universitats i Recerca del Dpt. d´Economia i Coneixement de la Generalitat de Catalunya (Ref. 2017SGR00773).

References

[1] Masselink, G., Russell, P., Turner, I. and Blenkinsopp, C., 2009. Net sediment transport and morphological change in the swash zone of a high-energy sandy beach from swash event to tidal cycle time scales. Marine Geology, Vol. 267: 18-35.

[2] Alsina, J.M., van der Zanden, J., Cáceres, I. and Ribberink, J.S., 2018. The influence of wave groups and wave-swash interactions on sediment transport and bed evolution in the swash zone. Coastal Engineering, Vol. 140, 23-42.

[3] Downing, J.P., Sternberg, R.W. and Lister, C.R.B., 1981. New instrumentation for the investigation of sediment suspension processes in the shallow marine environment. Marine Geology, Vol. 32, 19-34.

[4] D & A Instrument Company, 1991. Instruction Manual, OBS-1 and 3, p. 41.

[5] Butt, T., Miles, J., Ganderton, P. and Russell, P., 2002. A simple method for calibrating optical backscatter sensors in high concentrations of non-cohesive sediments. Marine Geology 192 (4), 419-424.

[6] Downing, J.P. and Beach, R.A., 1989. Laboratory apparatus for calibrating optical suspended solids sensors. Marine Geology, Vol. 86, 243–249.

[7] Downing, J.P. and Asher, W.E., 1997. The Effects of Colored Water and Bubbles on the Sensitivity of OBS Sensors. American Geophysical Union, 1997 Fall Meeting, San Francisco, CA.

[8] Terrill, E.J, Melville, W.K. and Stramski, D., 2001. Bubble entrainment by breaking waves and their influence on optical scattering in the upper ocean. Journal of Geophysical Research, Vol. 106, Nº C8, 16815-16823.

[9] Smith, G.G. and Mocke, G.P., 2002. Interaction between breaking/broken waves and infragravity-scale phenomena to control sediment suspension transport in the surf zone. Marine Geology, Vol. 187, 329–345.

[10] Puleo, J.A., Johnson, R.V., Butt, T., Kooney, T.N. and Holland, K.T., 2006. The effect of air bubbles on optical backscatter sensors. Marine Geology, Vol. 230: 87-97.

[11] Kalvoda, P.M., Xu, L and Wu, J., 2003. Macrobubble clouds produced by breaking wind waves: A laboratory study. Journal of Geophysical Research, Vol. 108, C6, 3207, doi:10.1029/1999JC000265

[12] Mori, N., Suzuki, T. and Kakuno, S., 2007. Experimental study of air bubbles and turbulence characteristics in the surf zone. Journal of Geophysical Research, Vol. 112, C05014, doi:10.1029/2006JC003647

[13] Bell, T.G., Landwehr, S., Miller, S.D., de Bruyn, W.J., Callaghan, A.H., Scanlon, B., Ward, B., Yang, M. and Saltzman, E.S., 2017. Estimation of bubble-mediated air-sea gas exchange from concurrent DMS and CO_2 transfer velocities at intermediate-high wind speeds. Atmospheric Chemistry and Physics, Vol 17, Pages: 9019-9033, doi:10.5194/acp-17-9019-2017.

[14] Chanson, H., Aoki, S. and Maruyama, M., 2002. Unsteady air bubble entrainment and detrainment at a plunging breaker: dominant time scales and similarity of water level variations. Coastal Engineering, Vol. 46, 139–157.

[15] Monahan, E. and Lu, M., 1990. Acoustically relevant bubble assemblages and their dependence on meteorological parameters. IEEE Journal of Oceanic Engineering, Vol. 15, Nº 4, 340-349. doi:10.1109/48.103530

[16] Deane, G. B., and Stokes, M. D., 2002. Scale dependence of bubble creation mechanisms in breaking waves. Nature 418, 839–844, doi:10.1038/nature00967

[17] Lamarre, E., 1993. An experimental study of air entrainment by breaking waves. PhD thesis, Department of Civil and Oceanographic Engineering. Cambridge, MA: MIT Press. doi: 10.1575/1912/5509

[18] Lamarre, E., Melville, W.K., 1992. Instrumentation for the measurement of void-fraction in breaking waves: Laboratory and field results. IEEE Journal of Oceanic Engineering, Vol. 17, Nº 2, 204–215. doi: 10.1109/48.126977

[19] Hall, K. R., 1990. Aeration in rubble-mound breakwater models. J. of Water, port, Coastal and Ocean Eng., ASCE, Vol. 116, pp. 400-405.

[20] Ting, F. C. K., and Kirby, J. T., 1995. Dynamics of surf zone turbulence in a strong plunging breaker, Coastal Engineering, Vol. 24, 177–204.

[21] Kiger, K.T. and Duncan, J.H., 2012. Air-Entrainment Mechanisms in Plunging Jets and Breaking Waves. Annual Review of Fluid Mechanics, Vol. 44, 563–596.

[22] van der A, D.A., van der Zanden, J., O'Donoghue, T., Hurther, D., Cáceres, I., McLelland, S. and Ribberink, J.S., 2017. Large-scale laboratory study of breaking waves hydrodynamics over a fixed bar. Journal of Geophysical Research: Oceans. Vol. 122(4), 3287-3310, doi:10.1002/2016JC012072

[23] van der Zanden, J., van der A, D. A., Cáceres, I., Hurther, D., McLelland, S.J., Ribberink, J. and O'Donoghue, T., 2018. Near-bed turbulent kinetic energy budget under a large-scale plunging breaking wave over a fixed bar. Journal of Geophysical Research: Oceans. Vol. 123, doi:10.1002/2017JC013411

[24] Battjes, J.A., 1974. Surf similarity. Proceedings of 14th Coastal Engineering Conference, Copenhagen, Denmark, 466–480.

[25] Smith, E. R., and Kraus, N. C., 1991. Laboratory study of wave-breaking over bars and artificial reefs. Journal ofWaterway, Port, Coastal, and Ocean Engineering, 117(4), 307–325. doi:10.1061/(asce)0733-950x(1991)117:4(307)

[26] Mori, N., Suzuki, T. and Kakuno, S., 2007. Noise of acoustic doppler velocimeter data in bubbly flow, J. Eng. Mech., 133(1), 122–125.

[27] Tucker, M.J. and Pitt, E.G., 2001. Waves in Ocean Engineering. Elsevier Ocean Engineering Book Series, Vol. 5, Amsterdam, 521 pp.

[28] Neumeier, U, 2006. Processing of wave data from pressure sensors. http://neumeier.perso.ch/matlab/waves.html.

[29] Goring, D.G. and Nikora, V.I., 2002. Despiking acoustic doppler velocimeter data. Journal of Hydraulic Engineering, 128(1): 117-126.

[30] Longuet-Higgins, M., 1953. Mass transport in water waves. Philosophical Transactions of the Royal Society A 245, 535-581. doi: 10.1098/rsta.1953.0006.

[31] Van den Bremer, T.S. and Breivik, O., 2017. Stokes drift. Philosophical Transactions of the Royal Society A, 376, 20170104. doi:10.1098/rsta.2017.0104

[32] Blenkinsopp, C.E. and Chaplin, J.R., 2007. Void fraction measurements in breaking waves. Proceedings of the Royal Society A., Vol. 463, 3151-3170, doi:10.1098/rspa.2007.1901.

[33] Lim, H., Chang, K, Huang, Z. and Na, B., 2015. Experimental study on plunging breaking waves in deep water. Journal of Geophysical Research, Vol. 120, 2007-2049, doi:10.1002/2014JC010269.

[34] Alsina, J.M., Padilla, E.M. and Cáceres, I., 2016. Sediment transport and beach profile evolution induced by bi-chromatic wave groups with different group periods. Coastal Engineering, Vol. 114, 325-340.

[35] Cáceres, I. and Alsina, J.M., 2012. A detailed, event-by-event analysis of suspended sediment concentration in the swash zone. Continental Shelf Research, Vol. 41, pp. 61-76.

[36] Chanson, H. and Lee, J.F., 1997. Plunging jet characteristics of plunging breakers. Coastal Engineering, Vol. 31, 125–141.

[37] Hwung, H. H., Chyan, J.M. and Chung, Y.C., 1992. Energy dissipation and air bubbles mixing insider the surf zone. International Conference on Coastal Engineering, 1992.

[38] Cartmill, J.W. and Su, M.Y., 1993. Bubbles size distribution under saltwater and freshwater breaking waves. Dynamic of Atmospheres and Oceans, Vol. 20, 25-31. doi:10.1016/0377-0265(93)90046-A.

[39] Anguelova, M.D. and Huq, P., 2018. Effects of salinity and bubble cloud characteristics. Journal of Marin Science and Engineering, Vol. 6, 1-17, doi:10.3390/jmse6010001

[40] Wu, J., 2000. Bubbles produced by breaking waves in fresh and salt waters. Journal of Physical Oceanography, Vol. 30, 1809-1813.